Nanoscale

PAPER

View Article Online
View Journal | View Issue

Cite this: *Nanoscale*, 2018, **10**, 1245

Optical trapping and optical force positioning of two-dimensional materials†

M. G. Donato, *[a] E. Messina,‡[a] A. Foti,[a] T. J. Smart,[b] P. H. Jones,[b] M. A. Iatì,[a] R. Saija,[c] P. G. Gucciardi[a] and O. M. Maragò *[a]

Received 30th August 2017,
Accepted 9th December 2017

DOI: 10.1039/c7nr06465a

rsc.li/nanoscale

In recent years, considerable effort has been devoted to the synthesis and characterization of two-dimensional materials. Liquid phase exfoliation (LPE) represents a simple, large-scale method to exfoliate layered materials down to mono- and few-layer flakes. In this context, the contactless trapping, characterization, and manipulation of individual nanosheets hold perspectives for increased accuracy in flake metrology and the assembly of novel functional materials. Here, we use optical forces for high-resolution structural characterization and precise mechanical positioning of nanosheets of hexagonal boron nitride, molybdenum disulfide, and tungsten disulfide obtained by LPE. Weakly optically absorbing nanosheets of boron nitride are trapped in optical tweezers. The analysis of the thermal fluctuations allows a direct measurement of optical forces and the mean flake size in a liquid environment. Measured optical trapping constants are compared with T-matrix light scattering calculations to show a quadratic size scaling for small size, as expected for a bidimensional system. In contrast, strongly absorbing nanosheets of molybdenum disulfide and tungsten disulfide are not stably trapped due to the dominance of radiation pressure over the optical trapping force. Thus, optical forces are used to pattern a substrate by selectively depositing nanosheets in short times (minutes) and without any preparation of the surface. This study will be useful for improving ink-jet printing and for a better engineering of optoelectronic devices based on two-dimensional materials.

1. Introduction

Two-dimensional, layered materials[1] form a large family of crystals having a multi-layer structure with strong in-plane covalent bonds between atoms and much weaker van der Waals interaction between layers. Graphene remains the prototypical structure for such materials,[2] but many other compounds, among which are hexagonal boron nitride (hBN), the transition metal dichalcogenides (TMDs, with the stoichiometry MX_2, M being a transition metal and X a chalcogen atom) and the transition metal oxides (TMOs), are actively studied for methods of synthesis,[3–5] and for the characterization[6–10] and applications[1,11–13] of these exciting materials. The synthesis method-of-choice depends largely on the best compromise between price and material quality with regard to the particular application. Liquid phase exfoliation[3] (LPE) has been already proved as a simple, large-scale method to exfoliate graphite[14] and other layered materials[4,5] down to mono- and few-layer flakes. The relative ease of production of these 2D atomic crystals *via* this method is a result of the asymmetry of the binding forces inside and between the layers.

Hexagonal boron nitride has a layered structure that on exfoliation produces nanosheets very similar to graphene, in which each C–C pair is replaced by a B–N couple with a bond length of 1.44 Å.[15] Due to these analogies, several studies[15] are in progress regarding the possibility of replacing graphene with hBN when its stronger thermal stability is required. Moreover, hBN is also one of the best electrically insulating thermal conductors, so its sheets have the potential for use as dielectric substrates for graphene and other layered materials in optoelectronic applications. It has also been reported that it can be used as a protective barrier for metals and as reusable substrates of Au particles for applications such as surface-

[a]*CNR-IPCF, Istituto per i Processi Chimico-Fisici, V.le F. Stagno D'Alcontres 37, I-98158 Messina, Italy. E-mail: maria.donato@cnr.it, onofrio.marago@cnr.it; Fax: +39 090 3974130; Tel: +39 090 39762249*

[b]*Department of Physics and Astronomy, University College London, London WC1E 6BT, UK*

[c]*Dipartimento di Scienze Matematiche e Informatiche, Scienze Fisiche e Scienze della Terra, Università di Messina, V.le F. Stagno D'Alcontres 31, I-98166 Messina, Italy*

†Electronic supplementary information (ESI) available: Optical characterization of exfoliated samples, optical trapping and metrology of boron nitride, calculation of optical forces in the dipole approximation, optical forces in the T-matrix formalism for non-spherical particles, Raman spectroscopy of pushed MoS_2 at 785 nm, supplementary videos. See DOI: 10.1039/C7NR06465A

‡Current address: CNR-ISMN, Instituto per lo studio dei materiali nanostrutturati, Via Salaria Km 29300, 00015, Monterotondo Stazione, Roma, Italy.

enhanced Raman spectroscopy (SERS).[16] Moreover, hBN is more than a simple dielectric: it is naturally hyperbolic, which could pave the way to its application in the hot field of metamaterials, where several interesting exotic effects have been observed.[17]

Molybdenum disulfide (MoS_2) and tungsten disulfide (WS_2) belong to the family of TMDs and, as such, their two dimensional version consists of a three-layered structure in which each layer of metal atoms (Mo or W) is sandwiched between two layers of sulphur atoms.[18] The physical property that drives the research on these materials is their energy bandgap, that is essential for the realization of thin electronic devices. Moreover, the bandgap switches from indirect to direct when the number of layers is reduced to one, which is particularly appealing for photonics,[19] optoelectronics[18] and energy storage[1] applications. A further interesting application is the realization of van der Waals heterostructures,[20] in which 2D layers of different origin can stack on top of each other. In this regard, crucial assistance could be provided by optical tweezers,[21,22] that have been already proved useful for the controlled manipulation of micro- and nano-sized objects.[23]

Optical trapping stems from the conservation of the electromagnetic momentum in the light–matter interaction.[22] The total force acting on a small (*i.e.*, much smaller than the optical wavelength) particle may be separated into the sum of two main contributions:[21] the *gradient force*, which in optical tweezers arises from the strong variation of light intensity when a laser beam is focused by a high numerical aperture objective, and the *scattering force*, proportional to the particle extinction cross section,[22] which tends to push the particle along the beam propagation direction. If the gradient force is stronger than the radiation pressure, the particle is trapped, namely, it is confined close to the beam focus by optical forces alone. The balance between trapping forces and propelling forces is connected to the structural (shape) and optical properties of the particle. In general, the optical trapping of nanoparticles is difficult, because the gradient force scales (approximately) as the particle volume, and is easily overwhelmed by thermal fluctuations.[23] Several strategies have been used to enhance the gradient force with respect to repulsive forces, based on increased particle polarizability[24–27] and hybridization,[28,29] on particle geometrical anisotropies,[30–35] or even on the use of non Gaussian beams, having special polarization states.[36–38] However, even when the trapping is unstable, optical forces can still help in manipulation: optical pushing of gold nanoparticles has been used for the all-optical stamping of substrates[39–41] and to form aggregates[42] that act as sensors for the high-sensitivity detection of molecular species directly in a liquid environment.

In this work, we show that optical tweezers can be used for optical trapping and optical force positioning of two-dimensional nanoparticles obtained by LPE. Combined force and Raman spectroscopy of optically trapped individual hBN nanosheets allows one to get information on the flake size and number of layers directly in a liquid environment. Experimental results on optical trapping are compared with T-matrix calculations of optical forces *versus* flake size, exploring its size scaling. Optical pushing of MoS_2 and WS_2 nanoparticles permits us to pattern simple substrates without the need for complex, costly or special preparation of the surface. We study the dynamics of the deposition by Raman and photoluminescence spectroscopy, excited by the pushing beam, revealing the time evolution of the flake aggregation.

2. Results and discussion

2.1. Two-dimensional materials

The layered material samples used in this work are obtained by LPE[4,5,43] in an aqueous environment (see the Methods section for further details). In brief, the procedure is based on the surfactant-assisted ultrasonication of the layered materials-water dispersions, where sodium cholate is used as the surfactant to stabilize the flakes, preventing their re-aggregation. We follow the protocols described in Smith *et al.*[5] that ensures a *Z*-potential of approximately −40 meV, which is an indicator of very good colloidal stability. Indeed, this is also observed in our samples that appear to be stable, with no visible re-aggregation, after several months. Tuning of surface charge has proved to be important for the increase of optical forces on very small nanoparticles.[44] While tuning the *Z*-potential of layered material dispersions might help in stabilizing the optical trapping of flakes below 100 nm size, we expect a change in *Z*-potential to have a negligible effect on our layered flakes that have a larger average size.

Once sonicated, the dispersions are centrifuged to remove the unexfoliated powder. After centrifugation, the supernatants are extracted and used for spectroscopy, metrology and pushing experiments. Lotya *et al.*[43] showed that there is a precise relationship between the average flake size, as measured from TEM analysis, and centrifugation rate. For our centrifugation rate (1500 rpm), this corresponds to a lateral flake size in the range 0.1–1 μm with a mean value of about 400 nm. The unexfoliated part of the mixtures is used to prepare reference bulk samples.

The final dispersions are inspected by UV-Vis spectroscopy (see Fig. S1a in the ESI†), giving extinction spectra which are in agreement with literature results.[5,43]

2.2. Optical trapping and flake metrology of hexagonal boron nitride

Raman spectroscopy of trapped flakes. The coupling of an optical tweezers setup to a monochromator allows the spectroscopy of the trapped objects[23,45] directly in a liquid environment. For this reason, Raman and photoluminescence tweezers are very appealing applications especially with regards to the study of biological samples as they may avoid the complications connected to the immobilization on a substrate. Moreover, spectroscopic methods are potentially extremely useful in the study of inorganic micro- and nanoparticles such as upconverting nanoparticles,[46] single-walled carbon nanotubes[47,48] (SWNTs), and graphene flakes.[35] For example when

aiming at sorting on the basis of their spectroscopic characteristics, SWNTs may be dispersed in an aqueous environment with the aid of surfactants.[49] Their Raman spectra, however, must be recorded on drop-cast samples, and re-aggregation phenomena cannot be avoided. A similar problem must be faced for graphene obtained by liquid-phase exfoliation.[35] In this case, Raman tweezers may help in the study of the yield in graphene monolayers of the exfoliation process,[23] as it is known that the Raman spectrum of monolayer graphene has a well-defined peak at a Raman shift of approximately Δ_0 = 2700 cm^{-1}, the shape of which is sensitive to the number of layers.[50]

The first order Raman spectrum of highly oriented hBN crystals is characterized by two modes at Raman shifts Δ_0 = 51.8 cm^{-1} and at Δ_0 = 1366.2 cm^{-1} due to the E_{2g} symmetry vibrations.[51,52] The low energy mode is due to the sliding motion of adjacent planes, while the high energy mode is due to the in-plane atomic vibrations of boron and nitrogen atoms.[51,52] In the case of flakes obtained by micromechanical cleavage, monolayer hBN shows a blue shift of up to Δ = 4 cm^{-1} of the high-energy Raman peak of the crystal, while bilayer samples, on the contrary, show a Δ = 1–2 cm^{-1} red shift.[7]

In our measurements, a tightly focused (by a NA = 1.3 objective) laser beam (7 mW at the sample) with 780 nm wavelength has been used to both trap and excite the Raman scattering of the hBN flakes. Several flakes have been trapped, and their Raman spectra are recorded. Each spectrum (see Fig. 2a) has been fit with a single Lorentzian peak plus a linear background. We obtained a distribution of the hBN peak Raman shifts (Fig. 2b) that is compatible[7] with the presence, in solution, of mono- (blue shift of the hBN peak between 2 and 4 cm^{-1}) and bilayer flakes (approximately 2 cm^{-1} red shift of the hBN peak). The data have been compared with the value registered, in the same experimental configuration, on a bulk hBN sample, obtained by drop-casting the sediment residue after the centrifugation of the exfoliated hBN aqueous solution.

Photonic force microscopy and flake metrology. In optical tweezers, optical forces on the trapped particle due to the interaction with the laser beam are measured by studying the Brownian motion of the particle in the confining optical potential, which for small displacements from equilibrium can be considered harmonic.[22] Here we first discuss the simple case of an optically trapped spherical particle and then we generalize the calibration protocol to the non-spherical case of the hBN flakes.

In the overdamped (inertialess) regime, the Langevin equation for a spherical particle reduces to:[53]

$$\frac{dx_i}{dt} = -\frac{k_i}{\gamma}x_i(t) + \xi_i(t), \quad (1)$$

where k_i are the trap spring constants in the directions x_i, γ is the friction coefficient and $\xi(t)$ a random displacement that is the consequence of Brownian motion.[22]

From tracking of the particle position fluctuations in the trap, we obtain the optical trap stiffnesses, k_i and the conversion factors, β_i, between experimental units of the tracking signal, in volts, and physical distance, in μm (see the ESI†). Among the various approaches,[22] here we use the method of the particle position autocorrelation functions (ACFs),

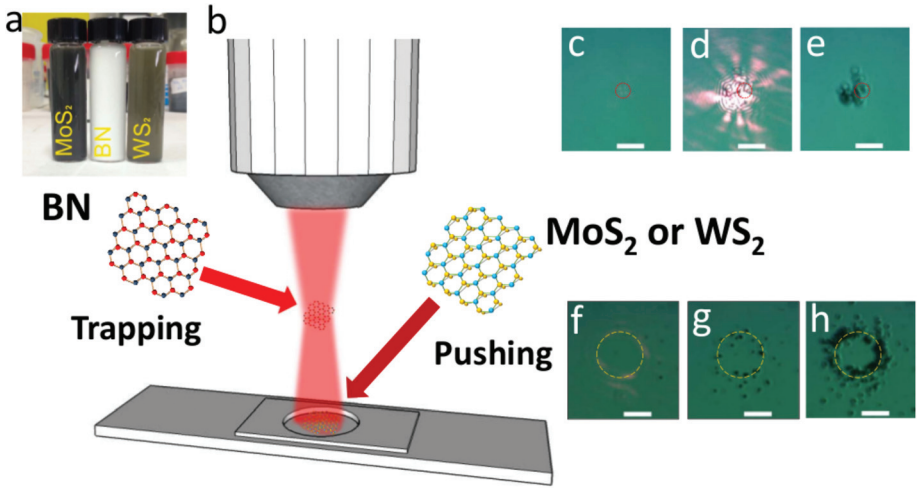

Fig. 1 (a) Aqueous dispersions of the 2D materials. (b) Sketch of the experimental setup. A high numerical aperture objective (NA = 1.3) is used to obtain a diffraction limited spot. Particles are trapped in the laser focus when the optical gradient force is greater than the scattering force. Conversely, the particles are optically pushed toward the bottom of the sample cell. If BSA is diluted in the aqueous medium, the particles stick to the walls of the cell and surface patterning is obtained. (c)–(e) Optical microscopy images recorded at the beginning of the pushing process of WS_2 with a Gaussian beam (c) and after approximately 90 seconds (d, e). In (d), the scattering of the laser light due to the formation of the WS_2 aggregate is clearly observed. The dashed circles are guides to the eye indicating the location of the beam waist. (f)–(h) Optical microscopy images registered at the beginning of the pushing process of MoS_2 (f) with a Laguerre-Gauss beam (l = 30), after approximately 2 minutes (g) and after approximately 18 minutes (h). The dashed circles are guides for the eye indicating the location of the high intensity doughnut beam (see also ESI Video 3†).

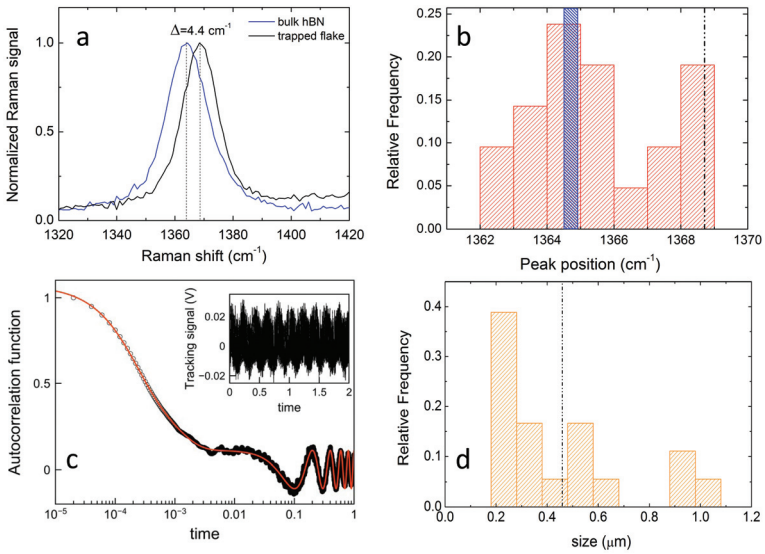

Fig. 2 Spectroscopy, trapping and metrology of hBN flakes. (a) Comparison between the Raman spectra of bulk hBN (blue curve) and trapped hBN monolayer (black curve). The blue shift Δ of the Raman peak of the monolayer with respect to the bulk value is also indicated. The exciting wavelength was λ = 780 nm. (b) Histogram of the Raman peak position of the trapped hBN flakes. The Raman peak positions Δ_0 = 1364.7 cm^{-1} and Δ_0 = 1368.6 cm^{-1} due to the bulk and the monolayer, respectively, are also indicated (blue bar and black dashed line). (c) Transverse signal autocorrelation function (black points) and its fit (red curve) with a double exponential decay plus a cosinusoidal oscillation at ω_{stage}. (d) Distribution of hBN flake size. The mean flake diameter d (dash-dot line) is approximately 460 nm. Bin size 100 nm, smallest diameter 180 nm.

which highlights the complex dynamics of non-spherical particles in the trap.[25,31,32,35] The ACF of position fluctuations for a spherical particle in a harmonic potential follows an exponential decay:[22]

$$C_{ii}(\tau) = \langle x_i(t)x_i(t+\tau)\rangle = C_{ii}(0)e^{-\omega_i\tau} = \frac{k_B T}{k_i}e^{-\omega_i\tau} \quad (2)$$

where $\omega_i = k_i/\gamma$ is the ACF relaxation frequency and the amplitude $C_{ii}(0)$ is obtained from energy equipartition.[22] In our experiments, the particle position is tracked *via* back focal plane interferometry,[54] and thus the detector used to track the particle displacements records voltage signals that are proportional to particle displacements $V_i(t) = \beta_i x_i(t)$. We must therefore calibrate the trap and the detector system in order to find the voltage-length conversion factor β_i.

Since the ACF of the tracking signal fluctuations is related to that of the position fluctuations as:

$$C_{ii}^{V}(\tau) = {\beta_i}^2 C_{ii}(\tau) = {\beta_i}^2 \frac{k_B T}{k_i}e^{-\omega_i\tau}, \quad (3)$$

then from the fit of the voltage ACFs we obtain both the trap spring constant k_i and the voltage-length conversion factor β_i. When the hydrodynamic radius, that for spherical particles generally coincides with the physical radius, R is known, the friction coefficient $\gamma = 6\pi\eta R$, where η is the viscosity of the suspending medium,[53] can be easily calculated and a full calibration of optical forces is achieved by the ACF analysis. However, when particle radius is not known, it is still possible to calibrate the trap and to obtain the estimation of the size of the trapped particle by applying a deterministic motion to the particle.[55,56] Here, we apply a controlled sinusoidal oscillation to the microscope stage:

$$x(t) = A_{stage}\sin(\omega_{stage}t), \quad (4)$$

where A_{stage} is the oscillation amplitude and ω_{stage} is the oscillation angular frequency. The trapped particle will thus be subjected to a similarly oscillating drag force

$$F_{drag} = -\gamma v_{stage} = -\gamma\omega_{stage}A_{stage}\cos(\omega_{stage}t), \quad (5)$$

and the tracking signal ACF will be:

$$C_{ii}^{V}(\tau) = Ae^{-\omega_i\tau} + \frac{{a_V}^2}{2}\cos(\omega_{stage}\tau) = {\beta_i}^2\frac{k_B T}{k_i}e^{-\omega_i\tau} + \frac{{a_V}^2}{2}\cos(\omega_{stage}\tau). \quad (6)$$

Here a_V is the amplitude of the oscillatory part of the tracking signal. In this case, the fit of the ACFs gives both the trap spring constants k_i and the calibration factors β_i. Additionally, the fit of the amplitude of the cosinusoidal oscillations provides a measure of the drag coefficients, from which it is possible to estimate the particle size (see the ESI† for details).

When the trapped particle is not spherical, simply using the hydrodynamic radius does not give the correct description of the particle dynamics in the trap. In fact, non-spherical particles are oriented in the trap by the optical torque[57,58] and different drag coefficients must be considered to correctly model the Brownian dynamics along the trap axes.[25,31,32,35] This is particularly important when dealing with high aspect ratio nanoparticles such as hBN flakes. Moreover, the anisotropic hydrodynamics and the possibility of particle orientational fluctuations must be considered. In this case, the ACFs

may show a double-exponential decay, since the tracking signal contains contributions from both translational and rotational motion on different timescales, which are fitted to obtain both force and torque constants.[25,31,32,35] Here we model our trapped hBN particles as extremely thin disks (of diameter d) parallel to the xz plane (where the axes are defined by the beam polarization, x, and the beam propagation, z, directions), and so we have to consider the drag coefficient $\gamma_{\perp} = \frac{16}{3}\eta d$ for particle displacements in the x and z directions (displacements perpendicular to the symmetry axis of the flake), and the drag coefficient $\gamma_{\parallel} = 8\eta d$ for displacements in the y direction.[35] Thus, in our experiments we measure these different drag coefficients and from each individual measurement we obtain an estimate of the trapped particle lateral size, d.

We oscillated the microscope stage in the x, y and z directions at $\omega_{stage} = 2\pi \times 5$ Hz and different amplitudes, depending on the strength of the optical trap. We measured the temperature of the sample chamber with a PT100 sensor to estimate the water viscosity η. We tracked the particle fluctuations using back focal plane interferometry, and calculated the corresponding ACFs. In Fig. 2c a transverse signal autocorrelation function (black points) and its fit (red curve) with a double exponential decay plus a cosinusoidal oscillation at 5 Hz is shown. In this case the double exponential is necessary due to the signal contributions from orientational fluctuations of the flake. The fits of ACFs for each measurement were used to obtain the decay constants, the calibration parameters and the drag coefficients. Finally, the hBN flake lateral size, d, and optical trap spring constants, k_i, were obtained for each trapped flake. The resulting distribution of hBN flake size is shown in Fig. 2d. We estimated that the mean flake diameter is approximately 460 nm (dash-dot line) in good agreement with the value of 400 nm as estimated from the TEM analysis of equivalent exfoliated samples in the literature[5,43] (see also section 2.1).

In order to understand the optical force size-scaling for the hBN bidimensional system in Fig. 3(a–c), the trap spring constants k_x (red squares), k_y (red circles) and k_z (red diamonds) measured for each trapped hBN flake are shown as a function of their measured lateral size d. The experimental data are compared with: (i) calculations of the trap spring constants based on the dipole approximation[22] (dashed green lines) for a flat spheroid[59] (see the ESI† for details), (ii) T-matrix calculations[57,58] (thick blue lines) for a thin (10 nm) planar cluster with increasing lateral size (see Methods and ESI†). To contrast the behaviour of the bidimensional system, we also show (purple lines) the results of Mie theory for spheres with the

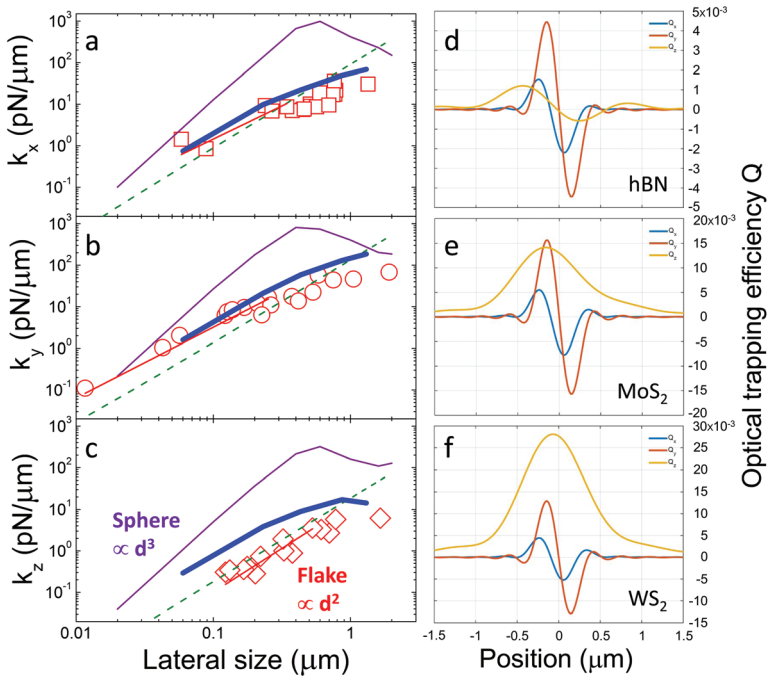

Fig. 3 (a–c) Optical trap force constants k_x (red squares), k_y (red circles) and k_z (red diamonds) measured for trapped hBN flakes as a function of their lateral size determined from the autocorrelation analysis (note the log–log scale). Optical force measurements are obtained at 830 nm with 26 mW power at the sample. Red lines are a power law fit to the small size data consistent a size scaling of d^2. Purple lines are Mie theory calculations for a sphere, following a d^3 scaling for small size. The dashed green lines represent the force constant estimates based on a simple dipole approximation (see the ESI†). Blue thick lines are T-matrix calculations for a planar cluster model of the hBN flake oriented in the xz plane because of optical torque. The agreement between experiments and T-matrix theory is excellent with no free parameters. (d–f) T-matrix calculations (830 nm, NA = 1.3) of optical force efficiencies, Q_x (light blue), Q_y (red), and Q_z (yellow) for 0.9 μm planar clusters of hBN (d), MoS_2 (e), and WS_2 (f). Note how Q_z has no zero for the case of MoS_2 and WS_2, hence trapping is not possible because of the strong absorption of these materials in the near-infrared.

same optical properties of hBN. At small flake size (smaller than the beam waist of about 300 nm), a scaling behaviour of the spring constants is observed. In fact, by fitting the data for small size with a power law (red lines in Fig. 3(a–c)), $k_i \propto d^{\alpha}$, we obtain $\alpha \approx 1.7$ in the transverse (k_x, k_y) direction and $\alpha \approx 2.1$ for the axial (k_z) one with an uncertainty of about 20%. This is consistent with the quadratic, $k_i \propto d^2$, behaviour expected from dipole approximation results related to the quadratic increase of the real part of the polarizability for a small flat spheroid (see the ESI†). In contrast, a spherical particle (purple lines) at small size follows the well-known volumetric behaviour.[22] However, when the flake size becomes comparable with the beam waist, optical forces tend to constant values, due to the saturation of the beam-particle interaction region. In this case, k_i changes its dependence with flake size, passing from an initial flattening to a progressive reduction at increasing d. We check this change of optical force behaviour at large flake size by an accurate modeling of optical trapping, for our experimental parameters (NA = 1.3, 830 nm, P = 26 mW), by using light scattering theory in the T-matrix approach[60,61] for a planar cluster model of the hBN flake oriented in the xz plane by the optical torque (thick blue lines in Fig. 3(a–c)). The agreement between experiments and T-matrix theory is excellent with no free parameters. The small discrepancy between the axial (k_z) experimental points with respect to T-matrix calculations is related to the unavoidable aberration of the oil-immersion objective used in the experiments that weakens the trap along the beam propagation (z) direction.[22]

2.3. Optical positioning of MoS_2 and WS_2

Optical pushing of particles becomes possible when the gradient force is not able to overcome the scattering force. MoS_2 and WS_2 have larger extinction coefficients than hBN,[4,7,62,63] which justifies the fact that in our experimental conditions, and at the wavelengths used, we do not trap MoS_2 and WS_2 flakes in three dimensions. These observations are supported by T-matrix calculations (see Methods and ESI†) of optical force efficiencies, $Q_i = cF_i/n_mP$ (i = x,y,z), for planar clusters shown in Fig. 3(d–f). Optical trapping occurs when Q_i vanish with a negative derivative.[58] A planar cluster of hBN (Fig. 3(d)) shows optical trapping in 3-D because the optical force efficiencies vanish in x,y,z. In contrast, a cluster with the same size but optical properties of MoS_2 (Fig. 3(e)) or WS_2 (Fig. 3(f)) show optical trapping only in the transverse directions (x,y), while it never shows a vanishing value of Q_z because of the strong absorption of these materials in the near-infrared resulting in a large increase of radiation pressure (see also the ESI† for a comparison using simple analytical dipole approximation results).

However, this large radiation pressure helps us with the positioning of these particles onto flat surfaces. As shown in Video 1,† we observe the 2D confinement of these flakes when the laser beam is focused near the microscope slide surface. In particular, we observe that MoS_2 and WS_2 flakes are pushed away from the laser focus when the beam is focused from the coverslip inside the sample chamber, until we reach the opposite surface. Here, the flakes are pushed towards the surface and cannot escape from the trap, since the transverse gradient forces confine them in the laser spot. However, when the laser is off, the particles are free to move and disperse in the medium. At higher power, the flakes are temporarily stuck to the surface, but the aggregate is unstable (see ESI Video 2†). Furthermore, thermal effects such as the creation of bubbles in the host medium are observed, due to material absorption.

Positioning with proteins. Recently,[42] optical aggregation of gold (Au) nanorods has been achieved to realize SERS sensors for proteins directly in a aqueous environment. Proteins in solution link to the Au nanorods, forming protein-nanorods complexes that under optical pushing are guided towards the substrate and create macroscopic aggregates. Here, we add a buffered Bovine Serum Albumin (BSA) aqueous solution to our MoS_2 and WS_2 dispersion, to help adhesion of the 2D flakes to the substrate and achieve controlled patterning of a substrate.

In Fig. 1(c–e), the formation of an aggregate of WS_2 + BSA on a standard, untreated, glass microscope slide obtained by optically pushing from aqueous solution with a Gaussian beam is shown. The formed WS_2 + BSA aggregate is stably adhered to the surface. Moreover, pattering of the substrate is possible by shaping the pushing beam intensity profile. In Fig. 1(f–h) and ESI Video 3† the formation of an annular pattern on the microscope slide is obtained by pushing the MoS_2 + BSA solution with a high-order (topological charge l = 30) ring-shaped Laguerre-Gauss (LG) beam[22,36] generated by a spatial light modulator (see Methods). LG beams are frequently used in optical tweezers experiments, both for the transfer of orbital angular momentum leading to controlled rotations,[36,64] and for the optical trapping of objects that are repelled from the high intensity part of the laser beam due to their optical properties.[65] Here, use of the LG beam acts as a proof of principle that more complex patterning beyond the clusters formed by a simple Gaussian beam is possible with appropriate beam shaping.

Spectroscopy and aggregate temporal evolution. Raman spectroscopy of MoS_2 and WS_2 has been used in recent studies as a tool to distinguish mono- and few-layer flakes from bulk crystals.[4,6,8–10] In fact, it has been observed that the first order Raman features due to the $E_{2g}{}^1$ and A_{1g} modes at approximately 382 and 408 cm^{-1} in MoS_2,[8,66] and at approximately 355.5 cm^{-1} and 420.5 cm^{-1} in WS_2 [9] approach each other in monolayer flakes, and move to the frequencies of the bulk when more than six layers are present in the flake. Moreover, in the case of a Raman excitation energy near to an absorption transition of the material, a resonant scattering process occurs, giving rise to a spectrum with several second order (*i.e.*, involving two phonons) features.[8,67]

We have studied the aggregation process of our 2D exfoliated materials by following the temporal evolution of their Raman spectra. We used an exciting wavelength (λ = 638 nm) that gives resonant Raman scattering in both materials. Each Raman spectrum has been recorded within ten seconds of laser pushing (see Methods). The spectra registered on MoS_2

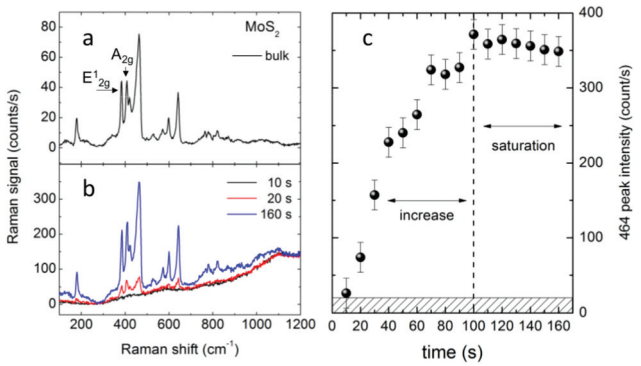

Fig. 4 Optical force aggregation of MoS_2. Raman spectra obtained on bulk MoS_2 (a) and under laser pushing of exfoliated MoS_2 at 638 nm (b). In (a), a long-working distance (LWD) ×50 objective (NA = 0.5) has been used, while in (b) a ×100 oil immersion objective (NA = 1.3) has been used. (c) Time evolution of 2LA(M) peak at $\Delta_0 \approx 464$ cm^{-1} shown in (b). A clear increase of the peak signal is observed in the first 100 s of the pushing process, followed by its stabilization and saturation, due to the complete filling of the sampling volume of laser beam.

aggregates at increasing deposition time are shown in Fig. 4b. Upon fitting, we found $E_{2g}{}^1$ peaks at Δ_0 = 383–384 cm^{-1}, and A_{1g} peaks between Δ_0 = 406 cm^{-1} and Δ_0 = 408 cm^{-1}. These values are consistent with those observed in few layer flakes[6] obtained by mechanical exfoliation, and, as also observed in samples obtained by LPE,[5] they are close to the values (~383 and ~407 cm^{-1}) obtained on the reference sample (Fig. 4a), which has been prepared with the residue at the bottom of the centrifugation cell.

The temporal evolution of the aggregate has been studied by focusing on the most prominent feature in the resonant Raman spectrum, *i.e.*, the peak at approximately Δ_0 = 464 cm^{-1} due to an overtone of a longitudinal acoustic (LA) phonon[66] at the *M* point (232 cm^{-1}). The spectrum obtained after the first ten seconds of pushing is featureless, but after twenty seconds (Fig. 4b) a small Raman signal is observed that is consistent with the results obtained in few-layer MoS_2 at the excitation wavelength λ = 633 nm.[8] The signal amplitude gradually increases, indicating the increase of the aggregate size. When the formed aggregate completely fills the sampling volume of the laser beam, the Raman signal saturates. In Fig. 4c, the time evolution of the 2LA(*M*) peak at 464 cm^{-1} clearly summarizes these results.

Note that we cannot discriminate a single particle increase for consecutive Raman spectra. This is because the large range in lateral flake size[5,43] (0.1–1 μm) in the dispersion is such that a single flake Raman signal can have a large variation in intensity and, in our ten seconds acquisition time, we cannot distinguish between the intensity of a single large flake or the signal from few small ones.

In the case of pushing with a non-resonant wavelength (λ = 785 nm), some differences between the spectra obtained on the exfoliated material and on the bulk can be observed (see the ESI†). All the features in the spectra of the pushed material can be explained on the basis of the phononic spectrum of MoS_2.[66] The great enhancement of the LA(*M*) peak at approximately 234 cm^{-1} with respect to the bulk could be explained by the presence of defects at the edges of our exfoliated flakes,[68] as is observed also in liquid exfoliated graphene flakes.[35] This could explain also the low amplitude of the $E_{2g}{}^1$ and A_{1g} peaks observed in the spectra of exfoliated materials when compared with the corresponding values in bulk.

A similar spectroscopic study of the pushing and aggregation process in exfoliated WS_2 has been carried out. In Fig. 5a and b, the Raman spectra obtained at λ = 638 nm exciting wavelength on bulk (Fig. 5a) and on a growing aggregate (Fig. 5b) are shown. All the Raman features can be explained on the basis of the phononic spectrum of the material. It is worth noting that at resonant Raman excitation a peak at approximately 350 cm^{-1}, due to an overtone of a LA(*M*) phonon, becomes more prominent, nearly overshadowing the $E_{2g}{}^1$ peak. Upon fitting, we cannot separate the contribution of these two peaks, that are convoluted. On the contrary, the A_{1g} peak is easily fit, giving values Δ_0 = 418–419 cm^{-1}, which are consistent[10] with the presence in solution of few-layer flakes. The spectra are overlapped to a broad background that can be associated with the low energy tail of a PL emission centered at 630 nm due to defects present at the edges of WS_2 monolayers of small size (<5 μm).[9,10] On the basis of these results, the dynamics of the aggregation process has been followed by focusing on this PL background (Fig. 5c) and on the Raman peak at 418 cm^{-1}. At increasing deposition time, an overall increase of both signals is observed, which is consistent with an average increase of the aggregate size. However, this process goes through a series of increasing-decreasing steps, that are more evident at higher laser power. This could be explained by supposing an annealing effect of the aggregate structure, which is interrupted when a new flake adds to the aggregate. Finally, it is worth noting that, because of its low concentration, the presence of BSA in solution does not alter the Raman spectra of the deposited materials.

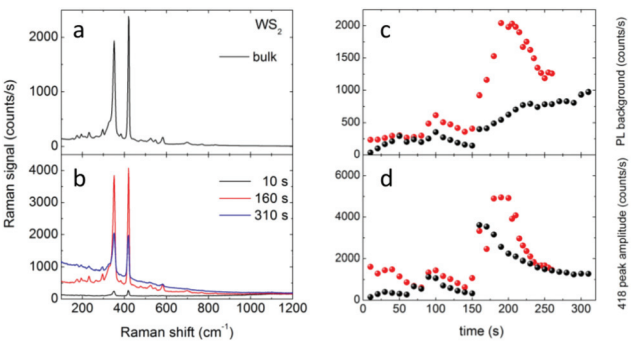

Fig. 5 Optical force aggregation of WS_2. On the left, Raman spectra obtained on bulk WS_2 (a) and under laser pushing of exfoliated WS_2 (b). For the spectrum of the bulk, the ×50 LWD objective has been used. On the right, the time evolution of the photoluminescence background (c) and of the $\Delta_0 \approx 417$ cm^{-1} Raman peak (d) of WS_2 for two different pushing powers (black dots, ~5 mW; red dots, ~17 mW) are shown. In these plots, the error bars are smaller than the data marker size. Exciting wavelength λ = 638 nm.

3. Conclusions

In conclusion, in this work we demonstrate that optical forces are powerful tools for the manipulation, positioning and characterization of liquid exfoliated 2D nanoparticles directly in their environment. On the one hand, optical trapping can be used for metrology of exfoliated hBN, to determine the size of few-layer flakes obtained in the deposition process. On the other hand, optical pushing can be used to pattern common substrates such as microscope slides with MoS_2 and WS_2. Importantly, both techniques can be combined with spectroscopic tools for material characterization, such as quantifying the number of layers in the flake. This could be particularly useful for the controlled patterning of substrates with layered materials or to realize mixed van der Waals structures with layered materials of different origin.

4. Methods

4.1. Liquid phase exfoliation of two-dimensional materials

The hBN, MoS_2 and WS_2 powders were purchased from Sigma Aldrich. In all cases, the starting material showed platelet shapes. The powders generally consist of flakes with lateral size of 1 μm in case of hBN and approximately 2 μm and 6 μm in WS_2 and MoS_2, respectively. The initial size of the microplatelets is important to obtain a high quality final product.[4,5] The layered compounds are dispersed in sodium cholate/water solution (0.045 mg mL^{-1}) at a concentration of 0.15 mg mL^{-1} through horn ultrasonication (Branson Sonifier 250) for 30 minutes. To reduce solvent heating and, thus, sample degradation, the dispersions were submerged in an ice bath. The sonication process results in dark green dispersions for MoS_2 and WS_2 and milky white dispersions for hBN (Fig. 1a). The dispersions are then transferred to a glass pot (40 mL) and allowed to decant overnight. Finally, the top part (20 mL) of the dispersions is centrifuged at about 1500 rpm (revolutions per minute) for 15 minutes so as to increase the amount of few-layered flakes.

4.2. Optical and Raman tweezers

Our optical and Raman tweezers are based on an inverted microscope configuration. Optical trapping and metrology of hBN flakes have been carried out using an exciting beam with wavelength 830 nm derived from a laser diode (Thorlabs DL8142-201). The laser beam, after the passage through an anamorphic prism pair, is expanded by using a 1 : 4 telescope. The resulting beam overfills the back aperture of a high numerical aperture (NA = 1.3) oil immersion objective and is focused to a laser spot ~600 nm in diameter. The power at the sample is approximately 26 mW. The sample chamber (volume 80 μL) is realized with a cavity well microscope slide, covered by using a No. 1.5 coverslip and sealed. The chamber is mounted on a nanopositioning system (Mad City Labs Nano-LP200) with a 200 μm range of motion on each x, y and z direction, at 0.4 nm resolution. A thermoresistive sensor (PT100) has been mounted on the chamber to monitor its temperature. Particle tracking and force sensing have been obtained through back focal plane interferometry,[53,54] where the interference pattern from the unscattered and scattered light by the trapped particle is collected onto a quadrant photodiode (QPD). For flake metrology, after trapping, a controlled sinusoidal oscillation at 5 Hz is imposed on the stage for x, y and z directions separately, and the tracking signals registered independently. Three measurements for each direction are carried out. Thus, the signal autocorrelation functions are calculated and fit as outlined in the main text. In general, a single exponential decay plus a cosinusoidal oscillation is used for fitting the signal along z. For the signals along x and y, a double exponential decay plus an oscillation is used. We repeated this procedure on eighteen different flakes.

Raman tweezers experiments are carried out on a different setup. A beam from a diode laser (Thorlabs DL7140-201S) at 780 nm, passing through an anamorphic prism pair, is enlarged by using a 1 : 2 telescope and delivered by means of a notch filter (Semrock NF03-785E-25) to the back aperture of a high numerical aperture (NA = 1.3) oil immersion objective and used for both trapping and excitation of the Raman response of the trapped flake. The laser power at the sample chamber is approximately 7 mW. The sample chamber is mounted on a piezostage (Physics Instruments, P-517.3 CL) with 1 nm resolution. The backscattered light passes through the notch filter, used for Rayleigh scattering removal, and is subsequently focused by using a 50 mm focal length lens onto a Horiba Jobin–Yvon Triax 190 spectrometer (190 mm focal length) equipped with a 1200 lines per mm grating blazed at 650 nm. A high sensitivity CCD (Horiba Jobin–Yvon Synapse) is used for signal detection. A beam splitter is inserted in the optical path to reflect 50% of the scattered light toward a CCD camera (Thorlabs USB 2.0, DCU223M), allowing for the visual inspection of the trapped particle. To evaluate the reference value of the E_{2g} Raman peak in bulk hBN for comparison with the Raman peaks from trapped flakes, a small amount of the highly concentrated hBN solution taken at the bottom of the centrifuge cell is put on a coverslip and spectra are registered by focusing the laser through the coverslip itself, in the same experimental configuration of trapping experiments. To avoid thermal shifts of the Raman peak, a laser power of approximately 0.7 mW is used.

4.3. Optical force positioning

Optical pushing and aggregation of MoS_2 and WS_2 flakes is performed in an experimental set-up using an inverted microscope (Zeiss Axiovert 40 CFL). A high numerical aperture oil immersion objective (NA = 1.3) focuses the incoming laser beam at 785 nm on the inner surface of the sample cell (Fig. 1b). A CMOS camera (Thorlabs DCC 1645C-HQ) is used to image the sample during the aggregation process. To create a circular pattern on the surface, we used an LG beam which has a doughnut-shaped intensity distribution. The LG beam with l = 30 topological charge used in Fig. 1f–h and in Video 3† is generated by a spatial light modulator (Hamamatsu

LCOS-SLM X10468-02). This device is used as a diffractive optical element to modulate the phase of the incoming laser beam. To this aim, a computer-generated holographic mask is projected on the SLM plane.[22] By means of two lenses (f = 750 mm and 300 mm), this plane is imaged onto the back focal plane of the objective. Thus, at the focal plane of the objective the Fourier transform of the SLM plane is obtained.[53]

4.4. Raman spectroscopy of positioned samples

Raman spectroscopy of the MoS_2 and WS_2 aggregation process by optical pushing is carried out by means of a Horiba Jobin–Yvon Xplora system at 638 and 785 nm. The sample chamber has been realized with a microscope slide, a ~120 μm adhesive spacer and a No. 1.5 coverslip. 10^{-4} M Bovine Serum Albumin (BSA) in phosphate buffer solution (200 mM) has been added to the layered material solution. All the pushing measurements have been carried out by focusing the laser spot on the inner microscope slide surface. The flakes entering the laser beam are pushed toward the surface and adhere to the glass surface. During the aggregation process, single-shot Raman spectra are sequentially collected with an acquisition time of 10 s. By using a 1200 lines per mm grating, a single spectral window is enough to cover the range 100–1200 cm^{-1} at both the wavelengths used. Data shown in Fig. 4b, c and 5b have been obtained with 638 nm excitation wavelength and at approximately 4.7 mW laser power at the sample, corresponding to an estimated irradiance of about 8×10^{10} W m^{-2} (calculated considering a diffraction limited spot). Aiming at a comparison, we used as reference the Raman spectra registered, at low laser power (0.35 mW), on samples obtained by drying a small amount of the unexfoliated fraction of the MoS_2 and WS_2 dispersions, taken at the bottom of the centrifuge tube.

4.5. T-matrix calculations

Optical forces on layered material flakes are calculated by solving the light scattering problem in the T-matrix formalism[60,61] for planar clusters (see also the ESI†). The incident fields are the tightly focused fields creating the optical tweezers with the same parameters of the optical trapping experiments. First, we calculate the incident focal fields for the high numerical aperture (NA = 1.3) objective lens by using the angular spectrum representation[58] in the absence of any particle. Thus, the radiation force and torque[57] exerted on the planar cluster flake within the focal region are calculated by integrating the time-averaged Maxwell stress tensor,[22] $\bar{T}_M$, on a large sphere of radius r surrounding the particle:[57,58]

$$\mathbf{F}_{rad} = r^2 \oint_\Omega \bar{T}_M \cdot \hat{\mathbf{r}} d\Omega, \quad (7)$$

$$\mathbf{T}_{Rad} = -r^3 \oint_\Omega (\bar{T}_M \times \hat{\mathbf{r}}) \cdot \hat{\mathbf{r}} d\Omega, \quad (8)$$

where the integration is over the full solid angle. The radiation force and torque are then expressed in terms of incident and scattered fields that can be expanded, respectively, in vector spherical harmonics[22] regular at the origin (Bessel multipoles) or at infinity (Hankel multipoles). Thus, the T-matrix for the scattering process[60,61] is defined as the linear operator that links the scattered expansion amplitudes to the incident ones. Finally, optical force and torque components are obtained by projecting the radiation force and torque vectors on the different coordinate axes, *e.g.*, $F_x = \mathbf{F}_{rad} \cdot \hat{\mathbf{x}}$ or $T_z = \mathbf{T}_{rad} \cdot \hat{\mathbf{z}}$, and calculating the corresponding numerical integral.[57,58] For the planar cluster model used for the case of layered materials, we exploit the T-matrix formulation of light scattering by a cluster of spheres[60,61] (see the ESI†) where the fields scattered by the spherical subunits composing the planar cluster are combined by means of the addition theorem of multipole fields through a translation matrix.[22]

Conflicts of interest

There are no conflicts to declare.

Acknowledgements

We acknowledge support from the 'Programma Operativo Nazionale Ricerca e Competitività' 2007–2013, Project PAC02L3-00087 SOCIAL-NANO and Project PON03PE-00214-2 DELIAS, MPNS COST Action 1205 'Advances in Optofluidics: Integration of Optical Control and Photonics with Microfluidic' and MP1302 'Nanospectroscopy'.

References

1 F. Bonaccorso, L. Colombo, G. Yu, M. Stoller, V. Tozzini, A. C. Ferrari, R. S. Ruoff and V. Pellegrini, *Science*, 2015, **347**, 1246501.
2 K. S. Novoselov, A. K. Geim, S. V. Morozov, D. Jiang, Y. Zhang, S. V. Dubonos, I. V. Grigorieva and A. A. Firsov, *Science*, 2004, **306**, 666–669.
3 K. Novoselov, D. Jiang, F. Schedin, T. Booth, V. Khotkevich, S. Morozov and A. Geim, *Proc. Natl. Acad. Sci. U. S. A.*, 2005, **102**, 10451–10453.
4 J. N. Coleman, M. Lotya, A. O'Neill, S. D. Bergin, P. J. King, U. Khan, K. Young, A. Gaucher, S. De, R. J. Smith, *et al.*, *Science*, 2011, **331**, 568–571.
5 R. J. Smith, P. J. King, M. Lotya, C. Wirtz, U. Khan, S. De, A. O'Neill, G. S. Duesberg, J. C. Grunlan, G. Moriarty, *et al.*, *Adv. Mater.*, 2011, **23**, 3944–3948.
6 C. Lee, H. Yan, L. E. Brus, T. F. Heinz, J. Hone and S. Ryu, *ACS Nano*, 2010, **4**, 2695–2700.
7 R. V. Gorbachev, I. Riaz, R. R. Nair, R. Jalil, L. Britnell, B. D. Belle, E. W. Hill, K. S. Novoselov, K. Watanabe, T. Taniguchi, *et al.*, *Small*, 2011, **7**, 465–468.
8 H. Li, Q. Zhang, C. C. R. Yap, B. K. Tay, T. H. T. Edwin, A. Olivier and D. Baillargeat, *Adv. Funct. Mater.*, 2012, **22**, 1385–1390.

9 H. R. Gutiérrez, N. Perea-López, A. L. Elías, A. Berkdemir, B. Wang, R. Lv, F. López-Urías, V. H. Crespi, H. Terrones and M. Terrones, *Nano Lett.*, 2012, **13**, 3447–3454.
10 A. Berkdemir, H. R. Gutiérrez, A. R. Botello-Méndez, N. Perea-López, A. L. Elías, C.-I. Chia, B. Wang, V. H. Crespi, F. López-Urías, J.-C. Charlier, *et al.*, *Sci. Rep.*, 2013, **3**, 1755.
11 K. S. Novoselov, V. Fal, L. Colombo, P. Gellert, M. Schwab, K. Kim, *et al.*, *Nature*, 2012, **490**, 192–200.
12 F. Torrisi, T. Hasan, W. Wu, Z. Sun, A. Lombardo, T. S. Kulmala, G.-W. Hsieh, S. Jung, F. Bonaccorso, P. J. Paul, *et al.*, *ACS Nano*, 2012, **6**, 2992–3006.
13 D. McManus, S. Vranic, F. Withers, V. Sanchez-Romaguera, M. Macucci, H. Yang, R. Sorrentino, K. Parvez, S.-K. Son, G. Iannaccone, K. Kostarelos, G. Fiori and C. Casiraghi, *Nat. Nanotechnol.*, 2017, **12**, 343–350.
14 Y. Hernandez, V. Nicolosi, M. Lotya, F. M. Blighe, Z. Sun, S. De, I. McGovern, B. Holland, M. Byrne, Y. K. Gun'Ko, *et al.*, *Nat. Nanotechnol.*, 2008, **3**, 563–568.
15 L. H. Li and Y. Chen, *Adv. Funct. Mater.*, 2016, **26**, 2594–2608.
16 X. Ling, W. Fang, Y.-H. Lee, P. T. Araujo, X. Zhang, J. F. Rodriguez-Nieva, Y. Lin, J. Zhang, J. Kong and M. S. Dresselhaus, *Nano Lett.*, 2014, **14**, 3033–3040.
17 A. Poddubny, I. Iorsh, P. Belov and Y. Kivshar, *Nat. Photonics*, 2013, **7**, 948–957.
18 Q. H. Wang, K. Kalantar-Zadeh, A. Kis, J. N. Coleman and M. S. Strano, *Nat. Nanotechnol.*, 2012, **7**, 699–712.
19 L. Britnell, R. Ribeiro, A. Eckmann, R. Jalil, B. Belle, A. Mishchenko, Y.-J. Kim, R. Gorbachev, T. Georgiou, S. Morozov, *et al.*, *Science*, 2013, **340**, 1311–1314.
20 A. K. Geim and I. V. Grigorieva, *Nature*, 2013, **499**, 419–425.
21 A. Ashkin, J. Dziedzic, J. Bjorkholm and S. Chu, *Opt. Lett.*, 1986, **11**, 288.
22 P. H. Jones, O. M. Maragò and G. Volpe, *Optical tweezers: Principles and applications*, Cambridge University Press, Cambridge, 2015.
23 O. M. Maragò, P. H. Jones, P. G. Gucciardi, G. Volpe and A. C. Ferrari, *Nat. Nanotechnol.*, 2013, **8**, 807–819.
24 A. Lehmuskero, P. Johansson, H. Rubinsztein-Dunlop, L. Tong and M. Kall, *ACS Nano*, 2015, **9**, 3453–3469.
25 E. Messina, M. G. Donato, M. Zimbone, R. Saija, M. A. Iatì, L. Calcagno, M. E. Fragala, G. Compagnini, C. D'Andrea, A. Foti, P. G. Gucciardi and O. M. Maragò, *Opt. Express*, 2015, **23**, 8720–8730.
26 O. Brzobohatý, M. Šiler, J. Trojek, L. Chvátal, V. Karásek, A. Paták, Z. Pokorná, F. Mika and P. Zemánek, *Sci. Rep.*, 2015, **5**, 8106.
27 S. E. S. Spesyvtseva and K. Dholakia, *ACS Photonics*, 2016, **3**, 719–736.
28 D. Spadaro, M. A. Iatì, M. G. Donato, P. G. Gucciardi, R. Saija, A. R. Cherlakola, S. Scaramuzza, V. Amendola and O. M. Maragò, *RSC Adv.*, 2015, **5**, 93139–93146.
29 D. Spadaro, M. A. Iatì, J. Perez-Pineiro, C. Vázquez-Vázquez, M. A. Correa-Duarte, M. G. Donato, P. G. Gucciardi, R. Saija, G. Strangi and O. M. Marago, *J. Phys. Chem. C*, 2017, 691–700.
30 P. J. Pauzauskie, A. Radenovic, E. Trepagnier, H. Shroff, P. Yang and J. Liphardt, *Nat. Mater.*, 2006, **5**, 97.
31 O. M. Maragò, P. H. Jones, F. Bonaccorso, V. Scardaci, P. G. Gucciardi, A. G. Rozhin and A. C. Ferrari, *Nano Lett.*, 2008, **8**, 3211–3216.
32 A. Irrera, P. Artoni, R. Saija, P. G. Gucciardi, M. A. Iatì, F. Borghese, P. Denti, F. Iacona, F. Priolo and O. M. Marago, *Nano Lett.*, 2011, **11**, 4879–4884.
33 P. J. Reece, W. J. Toe, F. Wang, S. Paiman, Q. Gao, H. H. Tan and C. Jagadish, *Nano Lett.*, 2011, **11**, 2375–2381.
34 A. A. R. Neves, A. Camposeo, S. Pagliara, R. Saija, F. Borghese, P. Denti, M. A. Iatì, R. Cingolani, O. M. Maragò and D. Pisignano, *Opt. Express*, 2010, **18**, 822–830.
35 O. M. Maragò, F. Bonaccorso, R. Saija, G. Privitera, P. G. Gucciardi, M. A. Iatì, G. Calogero, P. H. Jones, F. Borghese, P. Denti, V. Nicolosi and A. C. Ferrari, *ACS Nano*, 2010, **4**, 7515.
36 M. Padgett and R. Bowman, *Nat. Photonics*, 2011, **5**, 343–348.
37 M. G. Donato, S. Vasi, R. Sayed, P. H. Jones, F. Bonaccorso, A. C. Ferrari, P. G. Gucciardi and O. M. Maragò, *Opt. Lett.*, 2012, **37**, 3381–3383.
38 Z. Yan, J. E. Jureller, J. Sweet, M. J. Guffey, M. Pelton and N. F. Scherer, *Nano Lett.*, 2012, **12**, 5155–5161.
39 M. J. Guffey and N. F. Scherer, *Nano Lett.*, 2010, **10**, 4302–4308.
40 S. Nedev, A. S. Urban, A. A. Lutich and J. Feldmann, *Nano Lett.*, 2011, **11**, 5066–5070.
41 A. S. Urban, S. Carretero-Palacios, A. A. Lutich, T. Lohmüller, J. Feldmann and F. Jäckel, *Nanoscale*, 2014, **6**, 4458–4474.
42 B. Fazio, C. D'Andrea, A. Foti, E. Messina, A. Irrera, M. G. Donato, V. Villari, N. Micali, O. M. Maragò and P. G. Gucciardi, *Sci. Rep.*, 2016, **6**, 26952.
43 M. Lotya, A. Rakovich, J. F. Donegan and J. N. Coleman, *Nanotechnology*, 2013, **24**, 265703.
44 H. Rodríguez-Rodríguez, P. Rodriguez Sevilla, E. Martin Rodriguez, D. H. Ortgies, M. Pedroni, A. Speghini, M. Bettinelli, D. Jaque and P. Haro-González, *Small*, 2015, **11**, 1555–1561.
45 D. V. Petrov, *J. Opt. A: Pure Appl. Opt.*, 2007, **9**, S139–S156.
46 P. Rodríguez-Sevilla, H. Rodríguez-Rodríguez, M. Pedroni, A. Speghini, M. Bettinelli, J. G. Solé, D. Jaque and P. Haro-González, *Nano Lett.*, 2015, **15**, 5068–5074.
47 O. Maragò, P. Gucciardi and P. Jones, *Scanning Probe Microscopy in Nanoscience and Nanotechnology*, Springer, 2010, pp. 23–56.
48 S. E. S. Spesyvtseva, S. Shoji and S. Kawata, *Phys. Rev. Appl.*, 2015, **3**, 044003.
49 F. Bonaccorso, T. Hasan, P. Tan, C. Sciascia, G. Privitera, G. Di Marco, P. Gucciardi and A. Ferrari, *J. Phys. Chem. C*, 2010, **114**, 17267–17285.
50 A. C. Ferrari, J. Meyer, V. Scardaci, C. Casiraghi, M. Lazzeri, F. Mauri, S. Piscanec, D. Jiang, K. Novoselov, S. Roth, *et al.*, *Phys. Rev. Lett.*, 2006, **97**, 187401.

51 R. Nemanich, S. Solin and R. M. Martin, *Phys. Rev. B: Condens. Matter Mater. Phys.*, 1981, **23**, 6348.
52 S. Reich, A. Ferrari, R. Arenal, A. Loiseau, I. Bello and J. Robertson, *Phys. Rev. B: Condens. Matter Mater. Phys.*, 2005, **71**, 205201.
53 G. Pesce, G. Volpe, O. M. Maragó, P. H. Jones, S. Gigan, A. Sasso and G. Volpe, *J. Opt. Soc. Am. B*, 2015, **32**, B84–B98.
54 F. Gittes and C. F. Schmidt, *Opt. Lett.*, 1998, **23**, 7–9.
55 S. F. Tolić-Nørrelykke, E. Schäffer, J. Howard, F. S. Pavone, F. Jülicher and H. Flyvbjerg, *Rev. Sci. Instrum.*, 2006, **77**, 103101.
56 A. Buosciolo, G. Pesce and A. Sasso, *Opt. Commun.*, 2004, **230**, 357–368.
57 F. Borghese, P. Denti, R. Saija and M. A. Iatì, *Opt. Express*, 2006, **14**, 9508–9521.
58 F. Borghese, P. Denti, R. Saija and M. A. Iatì, *Opt. Express*, 2007, **15**, 11984–11998.
59 C. F. Bohren and D. R. Huffman, *Absorption and scattering of light by small particles*, John Wiley & Sons, 1998.
60 R. Saija, M. A. Iatì, F. Borghese, P. Denti, S. Aiello and C. Cecchi-Pestellini, *Astrophys. J.*, 2001, **559**, 993–1004.
61 R. Saija, M. A. Iatì, P. Denti, F. Borghese, A. Giusto and O. I. Sindoni, *Appl. Opt.*, 2003, **42**, 2785–2793.
62 C. Yim, M. O'Brien, N. McEvoy, S. Winters, I. Mirza, J. G. Lunney and G. S. Duesberg, *Appl. Phys. Lett.*, 2014, **104**, 103114.
63 S. Alfihed, M. Hossain, A. Alharbi, A. Alyamani and F. H. Alharbi, *J. Mater.*, 2013, **2013**, 603648.
64 N. Simpson, L. Allen and M. Padgett, *J. Mod. Opt.*, 1996, **43**, 2485–2491.
65 G. Memoli, C. R. Fury, K. O. Baxter, P. N. Gélat and P. H. Jones, *J. Acoust. Soc. Am.*, 2017, **141**, 3364–3378.
66 B. C. Windom, W. Sawyer and D. W. Hahn, *Tribol. Lett.*, 2011, **42**, 301–310.
67 J.-H. Fan, P. Gao, A.-M. Zhang, B.-R. Zhu, H.-L. Zeng, X.-D. Cui, R. He and Q.-M. Zhang, *J. Appl. Phys.*, 2014, **115**, 053527.
68 É. Blanco, P. Afanasiev, G. Berhault, D. Uzio and S. Loridant, *C. R. Chim.*, 2016, **19**, 1310–1314.